

EXPLORING MORPHOLOGICAL CORRELATIONS AMONG H₂CO, ¹²CO, MSX AND CONTINUUM MAPPINGSCHUAN PENG ZHANG^{1,2}, JARKEN ESIMBEK^{1,3}, JIAN JUN ZHOU^{1,3}, GANG WU^{1,3} & ZHI MAO DU^{1,2}

Draft version August 22, 2011

ABSTRACT

There are relatively few H₂CO mappings of large-area giant molecular cloud (GMCs). H₂CO absorption lines are good tracers for low-temperature molecular clouds towards star formation regions. Thus, the aim of the study was to identify H₂CO distributions in ambient molecular clouds. We investigated morphologic relations among 6-cm continuum brightness temperature (CBT) data and H₂CO (1₁₁ – 1₁₀; Nanshan 25-m radio telescope), ¹²CO (1–0; 1.2-m CfA telescope) and midcourse space experiment (MSX) data, and considered the impact of background components on foreground clouds. We report simultaneous 6-cm H₂CO absorption lines and H110 α radio recombination line observations and give several large-area mappings at 4.8 GHz toward W49 (50' \times 50'), W3 (70' \times 90'), DR21/W75 (60' \times 90') and NGC2024/NGC2023 (50' \times 100') GMCs. By superimposing H₂CO and ¹²CO contours onto the MSX color map, we can compare correlations. The resolution for H₂CO, ¹²CO and MSX data was \sim 10', \sim 8' and \sim 18.3'', respectively. Comparison of H₂CO and ¹²CO contours, 8.28- μ m MSX colorscale and CBT data revealed great morphological correlation in the large area, although there are some discrepancies between ¹²CO and H₂CO peaks in small areas. The NGC2024/NGC2023 GMC is a large area of HII regions with a high CBT, but a H₂CO cloud to the north is possible against the cosmic microwave background. A statistical diagram shows that 85.21% of H₂CO absorption lines are distributed in the intensity range from -1.0 to 0 Jy and the ΔV range from 1.206 to 5 km s⁻¹.

Subject headings: formation; massive; clouds; HII regions; imaging; individual (W49, W3, DR21/W75 & NGC2024/NGC2023)

1. INTRODUCTION

Absorption lines for formaldehyde (H₂CO; $J_{KaKc} = 1_{11} - 1_{10}$; $\nu_o = 4829.659$ 4MHz), discovered in the interstellar medium by Snyder et al. (1969), are commonly detected toward star formation regions. H₂CO is a slightly asymmetric rotor molecule and is inherently sensitive to kinetic temperature. H₂CO is an accurate probe of physical conditions in dense molecular clouds (Mangum & Wootten 2002). Anomalous absorption lines can be seen against the 2.7 K cosmic microwave background (CMB; Palmer et al. 1969) and detected in dark clouds. Absorption is strongest at high density and temperature owing to the collisional pumping mechanism. A survey by Downes et al. (1980) between $l = 0^\circ$ and 60° , $b = \pm 1^\circ$ suggested that HII regions are associated with H₂CO. 12 bright galactic HII regions and two dark clouds (W3, W3(OH), NGC2024, W31, W33, M17, W43, W49A, W51A, W51B, K3-50 and DR21/W75; NGC2264 and Heiles cloud 2) have been mapped at an angular resolution of 2.6' using a 100-m telescope (Bieging et al. 1982), but their mapping areas are smaller than ours. Toward L1551, observations made using the Arecibo Telescope showed that H₂CO lines not only trace the outer envelope or quiescent state of molecular clouds, but also provide kinematic information on star formation (Araya et al. 2006). Piepenbrink & Wendker (1973) presented a first extensive survey of the Cyg X-region using H₂CO and H110 α lines as measured with the 100 m-RT Effelsberg telescope. Heiles clouds 1 and 2 and Lynds cloud L134 were mapped using the Onsala 25-m telescope and the results show that H₂CO contours generally coincide with ar-

eas of optical obscuration (Sume et al. 1975). Rodríguez et al. (2006) carried out a blind search of anomalous H₂CO absorption lines in the general direction of the galactic anticenter radiation using the Onsala 25-m radio telescope. This large-area mapping shows that H₂CO absorption and ¹²CO emission lines spatially coexist and all H₂CO absorption features observed are associated with known ¹²CO emission. In addition, Rodríguez et al. (2007) mapped a large region around L1204/S140 using H₂CO absorption line as measured with the Onsala 25-m telescope and concluded that ¹²CO emission and H₂CO absorption lines correlate fairly well, both qualitatively and quantitatively. Nevertheless, large-scale mappings of star formation regions using H₂CO absorption lines, especially for large-area GMCs, are relatively few.

McKee & Ostriker (2007) offered a basic description of turbulence, magnetic fields and self-gravity for the key dynamic processes involved in star formation. These three mechanisms influence the systematic velocity and broaden the line width. In general, most massive star formation regions deposit ultra-compact HII (UCHII) regions, which are dense and compact bubbles of photoionized gas of less than 0.1 pc in diameter and are surrounded by massive young stellar objects (YSOs; Thompson et al. 2006). Measurement of H110 α radio recombination lines (RRLs; $\nu_o = 4874.157$ MHz) and H₂CO absorption can be used to determine the kinematic distance of UCHII regions (e.g. Araya et al. 2002; Westerhout 1958). To discern the overall structure of GMCs, correlations among various molecular clouds should be considered and large-scale surveys are necessary.

In this paper, we report large-scale mappings of W49, W3, DR21/W75 and NGC2024/NGC2023 GMCs, almost all of which have a thermal background. We compare the relations among H₂CO, ¹²CO and MSX data and the continuum brightness temperature (CBT). The remainder of the paper is organized as follows. Section 2 describes the observations, data

¹ Xinjiang Astronomical Observatory, Chinese Academy of Sciences, Urumqi, 830011, China; zcp0507@gmail.com.

² Graduate University of the Chinese Academy of Sciences, Beijing, 100080, China.

³ Key Laboratory of Radio Astronomy, Chinese Academy of Sciences, Urumqi, 830011, China.

production and relevant parameters. In Section 3, we presents mappings for H_2CO , ^{12}CO , MSX and CBT data. In addition, we report some associations among ^{12}CO , H_2CO and continuum spectra, and define ranges for relations between line width and intensity. Finally, conclusions are presented in Section 4.

2. OBSERVATIONS AND DATA

2.1. Observations

Observations were made discontinuously from October 2009 to January 2011 using the Urumqi Nanshan 25-m telescope, which affords a half-power beam size (HPBW) of approximately $10'$ at 4.8 GHz. H_2CO absorption and $\text{H}110\alpha$ RRL spectra were simultaneously obtained using a 4096-channel digital autocorrelation spectrometer at a bandwidth of 80 MHz using position switching. The central velocity was $V_{LSR} = 0.0 \text{ km s}^{-1}$, the frequency was $F_{center} = 4851.9102 \text{ MHz}$, and the velocity channel width was 1.206 km s^{-1} . To achieve a better signal-to-noise ratio (S/N), the ON-source integration time was tens of minutes to up to several hours. CBT data at 4.8 GHz were processed with a bandwidth of about 400 MHz. The CBT error was approximately 1% and sensitivity was approximately 75 mJy. The system temperature during observations was 23 K. A diode noise source was used to calibrate the spectra and the flux error was 15%. The pointing accuracy was better than $15''$ for all observations and the antenna efficiency was 62%. The DPFU (degrees per flux unit) value was 0.116 K Jy^{-1} .

2.2. Data Reduction

Data reduction for H_2CO absorption lines and $\text{H}110\alpha$ RRLs was performed using CLASS and GREG, which are part of the GILDAS software developed by IRAM. Furthermore, $8.28\text{-}\mu\text{m}$ mid-infrared MSX archive data were handled using SAOImage DS9, Adobe Photoshop 7.0.1, Origin 8 and Adobe Illustrator CS software. Starlink software was used to process ^{12}CO cube data (Dame et al. 2001) to obtain parameters (integration intensity, velocity, intensity and line width) for comparison with H_2CO parameters.

2.3. Data Exhibition

MSX data traces star formation regions, and mainly traces the dust continuum emission from core, so that we could compare the distributional relation between H_2CO and MSX data, and shed light on the background environment for star formation regions, CBT data at 4.8 GHz and MSX data for the $8.28\text{-}\mu\text{m}$ band were used as the background for H_2CO contours. The correlation between MSX colorscale images and H_2CO absorption contours is described in Section 3. The 2.6-mm ^{12}CO data from the 1.2-m CfA telescope (Dame et al. 2001) were used as a background to determine their relationship. The CO beam size was $\sim 8'$, which is comparable to that for H_2CO ($\sim 10'$).

The optical depth, column density and mass for measured H_2CO absorption lines were calculated in the usual way. According to Bieging et al. (1982), the apparent optical depth is

$$\tau_{app} = -\ln\left[1 + \frac{T_L}{T_c + T_{bgd} - T_{ex}}\right], \quad (1)$$

where T_L is the line intensity measured, T_c is the CBT and T_{bgd} is the 2.7 K cosmic background temperature. T_{ex} is the

1.7 K excitation temperature of the H_2CO $1_{10} - 1_{11}$ transition. The H_2CO column density was calculated at the 1_{11} level as:

$$N(\text{H}_2\text{CO}) = 9.4 \times 10^{13} \tau_{app} \cdot \Delta V, \quad (2)$$

where ΔV is the H_2CO FWHM in km s^{-1} . Thus, the column density is (Scoville & Solomon 1973):

$$N(\text{H}_2) = 0.8 \times 10^9 N(\text{H}_2\text{CO}). \quad (3)$$

Finally, we used the following equation (Poeppel et al. 1983)

$$M(\text{H}_2) = S \cdot \overline{N(\text{H}_2)} \cdot m_{\text{H}_2} \cdot r^2 \quad (4)$$

to indirectly derive the clump's H_2 -mass:

$$M(\text{H}_2) = 1.36 \times 10^{-21} \cdot \frac{S}{(\text{arcmin})^2} \cdot \overline{N(\text{H}_2)} \cdot M_{\odot} \cdot r^2, \quad (5)$$

where S is the observational area, $\overline{N(\text{H}_2)}$ is the average column density, m_{H_2} is the mass of the H_2 -molecular and r (kpc) is their distances.

Table 1 lists ID numbers corresponding to the (0, 0) offset position in Figs. 1, 2, 3 and 4 for the four sources. Columns 3 and 4 show equatorial coordinates for the (0, 0) offset position. The distance in Column 5 comes from references (1, 2, 3 and 4) in Column 10. The size ($\alpha \times \delta$) in Column 6 is the approximate survey region, which is much larger than in previous studies. Column 7 lists the H_2 clouds mass and Column 8 the total integration time in the ON-position for every point source. In Column 9, A is the number of all observational positions toward the sources, B is the number of H_2CO absorption lines, and C is the number of $\text{H}110\alpha$ RRLs. Hence, the detection rate is 56.95% for H_2CO absorption lines and 10.60% for $\text{H}110\alpha$ RRLs.

Figs. 1, 2, 3 and 4 present spectral mosaics of H_2CO absorption lines and $\text{H}110\alpha$ RRLs toward W49, W3, DR21 and NGC2024 GMCs. The relative observational positions and the corresponding parameters are listed in Tables 2, 3, 4 and 5. The offset position is indicated on the relative coordinate axis and the step size is $10'$. The velocity components were identified by Gaussian fitting. All spectra are included, regardless of whether they contain signals. There are many blank panels for which sources could not be detected. Finally, all H_2CO absorption lines exhibited are stronger than 3σ in intensity. However, some of the $\text{H}110\alpha$ RRLs did not reach 3σ in intensity, as denoted by a in Tables 2, 3, 4 and 5. For faint ($< 3\sigma$) $\text{H}110\alpha$ RRLs, the spectra are shown for information only and were not studied further.

Tables 2, 3, 4 and 5 list the relevant parameters for H_2CO absorption lines and $\text{H}110\alpha$ RRLs. The serial number and coordinate offset are listed in Columns 1 and 2 for the corresponding spectral mosaics (Figs. 1, 2, 3 and 4). Columns 3–6 lists parameter data for H_2CO absorption lines, while those for $\text{H}110\alpha$ RRLs are in Columns 11–14. Columns 3 and 11 list line-of-sight velocity data relative to the Sun. Columns 4 and 12 list the integration intensity flux for each velocity component. Columns 5 and 13 list line width (FWHM) data with ΔV . Columns 6 and 14 list spectral intensity data. Columns 7–10 list the CBT at 4.8 GHz, the H_2CO optical depth, and the H_2CO and H_2 column density, respectively. The optical depth (τ_{app}) range is approximately 0.007–0.188, so H_2CO is optically thin. The column density ($N(\text{H}_2\text{CO})$) range is approximately $0.121 \times 10^{13} \text{ cm}^{-2}$ – $3.59 \times 10^{13} \text{ cm}^{-2}$. In addition, N indicates that the corresponding spectra could not be detected. $\text{H}110\alpha$ RRL data with a signal intensity of $< 3\sigma$ are denoted by a .

Fig. 5 shows an overlay of the integration intensity for H_2CO and ^{12}CO contours onto the 8.28- μm MSX color map. And, several representative objects are indicated in the maps. From Fig. 5, we find that the large area distributions of them are consistent, but there are some off-peak discrepancy between ^{12}CO peaks and others. We also compare the relations between velocity (Fig. 8), integration intensity (Fig. 9), intensity (Fig. 10) and line width (Fig. 11) to look for the relations between H_2CO and ^{12}CO . Moreover, we also overlay the H_2CO contours onto the 4.8 GHz continuum temperature contours in Fig. 6. From Fig. 6, we find that there is a good consistent morphologic distribution between H_2CO and CBT, and we also made a relation (Fig. 7) between integration intensity of H_2CO and CBT to derive a formula (Eqn. 6). Based on above, we suggest that H_2CO contours are more strongly correlated with the distribution of the continuum components than ^{12}CO , so that it is possible to produce the off-peak discrepancy. The character of these four GMCs is analyzed in Section 3.

3. RESULTS AND DISCUSSION

3.1. GMC descriptions

3.1.1. W49 GMC

The W49 GMC radio source was discovered in a 21-cm continuum survey by Westerhout (1958). The W49 GMC complex consists of a thermal component (W49A) and a non-thermal component (W49B). W49A is one of the most luminous galactic giant radio HII regions (Dreher et al. 1984; de Pree et al. 1997), and W49B is a supernova remnant (SNR). W49B and W49A are separated by 12.5' along an east-west line at a kinematic distance of 11.4 kpc (Gwinn et al. 1992). At this distance, $10' = 33.16$ pc. A giant-scale area (approx. $50' \times 50'$) was surveyed toward W49 GMC. During 966 minutes of integration, we observed five H_2CO absorption lines and two $\text{H}110\alpha$ RRLs. In our spectra (Fig. 1(a)), three H_2CO components of ~ 15.9 , ~ 40.9 and ~ 64.3 km s^{-1} were detected. Brogan & Troland (2001) mapped the HII region of W49A and W49B with 21-cm HI data, which revealed velocities of ~ 4 and ~ 7 km s^{-1} toward W49A, and ~ 40 and ~ 60 km s^{-1} toward W49A and W49B. H_2O emission lines were also observed at ~ 39 and ~ 60 km s^{-1} in W49A (Buhl et al. 1969). Furthermore, three absorption features at velocities of ~ 15 , ~ 40 and ~ 60 km s^{-1} were found for 18-cm OH absorption lines (Pastchenko & Slysh 1973). It is possible that the W49 GMC has an intricate kinematic structure or different velocity subclouds piled up in the line of sight. The multiple velocity components may arise from the Sagittarius spiral arm clouds (Brogan & Troland 2001). There is no clear evidence that W49B is closer to the Sun than W49A. However, many researchers are interested in whether W49A and W49B are physically correlated. Considering the uniform velocity components ~ 4.5 , ~ 10.5 , ~ 15.9 , ~ 40.9 and ~ 64.3 km s^{-1} from W49A and W49B, a physical association between them can be inferred.

3.1.2. W3 GMC

W3 GMC, at 1.95 kpc from the Sun (Xu et al. 2006), lies to the western edge of W4 GMC. At this distance, $10' = 5.672$ pc. W3 GMC is made up of three knots of molecular gas known as W3 Main, W3 North, and W3 OH. The Central Cluster, located between W3 Main and W3 OH, contains a large number of Class II YSOs (Ruch et al. 2007). A giant-scale area (approx. $70' \times 90'$) was surveyed toward W3 GMC.

We detected 19 H_2CO absorption lines and four $\text{H}110\alpha$ RRLs during 2370 minutes of integration. The W3 GMC is a complex of massive star formation regions, where there are strong H_2CO absorption lines, $\text{H}110\alpha$ RRLs, ^{12}CO emission lines, MSX sources and a CBT. We can clearly distinguish two cores for W3 GMC. At the junction (W3(OH)) of the two clouds, we cannot detect H_2CO absorption lines and the CBT is low, but the integration intensity for ^{12}CO clouds and MSX sources is relatively strong. We hypothesize that many young stars in W3(OH) are surrounded by a thin gas envelope. The velocity for H_2CO and $\text{H}110\alpha$ ranges from approximately -46.0 to -35.0 km s^{-1} , which is similar to HI observations (Read 1981). Table 3 reveals a strange phenomenon: a sharp velocity gradient is apparent, which is consistent with $J = 1-0$ ^{12}CO observations (Thronson et al. 1985). From northwest to southeast, the velocity varies strongly from -35.02 km s^{-1} (No. 08) to -45.14 km s^{-1} (No. 37) (Fig. 2(a) and Table 3).

3.1.3. DR21/W75 GMC

DR21/W75 GMC is located in the Cygnus constellation, approximately 3.0 kpc from the Sun (Campbell et al. 1982). At this distance, $10' = 8.727$ pc. The MSX color map reveals that DR21/W75 GMC exhibits a complex and dispersive structure, with many separate subclusters assembled together. We surveyed DR21 and W75 GMCs, which include W75N, W75, DR21(OH), DR21, L906E and Diamond Ring (source name). DR21 and W75 GMCs are associated with massive dense cores and are separated by approximately $30'$ (Wilson & Mauersberger 1990; Shirley et al. 2003). A giant-scale area (approx. $60' \times 90'$) was surveyed toward DR21/W75 GMC. We detected 34 H_2CO absorption lines and 8 $\text{H}110\alpha$ RRLs during 2742 minutes of integration. The velocity components are multiple and rather intricate (Fig. 3(a)). The velocity is smaller for the northeastern and larger for the southwestern section than for the central section. A velocity gradient exists within these subclouds, and probably arises from GMC rotation. A UCHII region was detected using $\text{H}110\alpha$ RRLs as a tracer. The data in Table 4 reveal that the $\text{H}110\alpha$ RRL intensity is so weak (indicated by *a*) that we could not obtain a good signal, even with long-time integration. In addition, we only detected part of the DR21/W75 GMC. In particular, for the western part there is a giant and strong MSX region, while the ^{12}CO cloud is relatively faint. To determine whether or not there is association between H_2CO and ^{12}CO clouds and MSX sources, the western edge of the DR21/W75 GMC should be observed.

3.1.4. NGC2024/NGC2023 GMC

NGC2024/NGC2023 GMC is situated in Orion B at a distance of 415 pc (Menten et al. 2007). At this distance, $10' = 1.207$ pc. The NGC2024/NGC2023 GMC is a bright emission nebula crossed by a prominent dust lane. NGC2024 GMC includes a number of protostars along the star-forming ridge extending in a north-south direction coincident with an HII region, which is in front of filamentary shaped dense molecular material (Gaume et al. 1992). A giant-scale area (approx. $50' \times 100'$) was surveyed toward NGC2024/NGC2023 GMC. The area has similar velocity components and integration intensity contours to those reported by Cohen et al. (1983), but our observational instrument was more sensitive than theirs. We detected 28 H_2CO absorption lines and two $\text{H}110\alpha$ RRLs during 3378 minutes of integration. The H_2CO velocity is approximately 11.70 km s^{-1} and comprises a single component

(Table 5). To the north of NGC2024/NGC2023, no strong infrared background can be detected and both the NRAO/VLA Sky Survey radio contour plot and the CBT at 4.8 GHz are much fainter than in the central section, whereas H_2CO absorption and ^{12}CO emission lines are widely distributed in this area. Hence, it is possible that the northern H_2CO absorption lines arise from CMB excitation.

3.2. Comparison of H_2CO distributions and the CBT

It is well known that the H_2CO absorption is strongly biased by the high CBT which is being absorbed by the H_2CO molecules along the line of sight to the source of the continuum. Here we will give the empirical relationship between H_2CO and CBT. In Fig. 6, continuum contours are overlaid on the H_2CO contour maps for W49, W3, DR21 and NGC2024 GMCs. The morphology of the H_2CO and continuum distributions matches very well. The H_2CO peaks are biased to the CBT peaks. For the offset(0, 0) positions of four GMCs, the CBTs are so high that H_2CO maybe mainly come from the CBT collision excitation. According to Tables 2, 3, 4 and 5, the H_2CO column density shows an irregular distribution that does not match the morphology of H_2CO intensity contours. By comparing the integration intensity contours for H_2CO with the CBT for GMCs (Fig. 7) and by polynomial fitting, we obtained the following equation:

$$\text{Flux}(\text{H}_2\text{CO}) = 0.70457 + 0.4834T_c + 0.15701T_c^2, \quad (6)$$

where $\text{Flux}(\text{H}_2\text{CO})$ is integration intensity of H_2CO , and T_c is 6-cm CBT. This further suggests in quantity that the H_2CO intensity is strongly influenced by the CBT background and that the contribution of CMB excitation to the intensity is very weak.

3.3. Comparison of H_2CO , ^{12}CO and MSX data

The velocity correlation between H_2CO and ^{12}CO is described in Fig. 8 for W49, W3, DR21 and NGC2024 GMCs. The fitting line passes through (0, 0) and the points are distributed almost on or near the line.

The correlations of integration intensity between H_2CO and ^{12}CO are plotted in Fig. 9 (ignoring these points of $|\text{Flux}(\text{H}_2\text{CO})| > 5 \text{ Jy km s}^{-1}$) for W3, DR21 and NGC2024 GMCs. The best least-squares fit to a straight line for W3, DR21 and NGC2024 GMCs GMC data sets yield respectively

$$\begin{aligned} \text{W3 : } \text{Flux}(\text{H}_2\text{CO}) &= 5.64 \times 10^{-3} \text{Flux}(^{12}\text{CO}) \\ &+ 65.59 \times 10^{-3} \text{K km s}^{-1}, \end{aligned} \quad (7)$$

$$\begin{aligned} \text{DR21 : } \text{Flux}(\text{H}_2\text{CO}) &= 4.25 \times 10^{-3} \text{Flux}(^{12}\text{CO}) \\ &+ 44.36 \times 10^{-3} \text{K km s}^{-1}, \end{aligned} \quad (8)$$

$$\begin{aligned} \text{NGC2024 : } \text{Flux}(\text{H}_2\text{CO}) &= 0.74 \times 10^{-3} \text{Flux}(^{12}\text{CO}) \\ &+ 80.48 \times 10^{-3} \text{K km s}^{-1}. \end{aligned} \quad (9)$$

Fig. 9 shows that the integration intensity relation between H_2CO and ^{12}CO for three GMCs is scattered. And the equation coefficients are different but similar between Rodríguez et al. (2007) and our results. It is suggested that there exists different physical condition for different GMCs, however, the correlation between H_2CO and ^{12}CO is inherent.

Fig. 10 shows the intensity correlation for H_2CO and ^{12}CO (ignoring these points of $|\text{Intensity}(\text{H}_2\text{CO})| > 1.2 \text{ Jy}$). For

W3, DR21 and NGC2024 GMCs, the correlation coefficient is 0.558, 0.499 and 0.297, respectively. Thus, the linear relation is better for W3 and DR21 GMCs than for NGC2024. The reason may be that H_2CO absorption to the north of the NGC2024 GMC arises from CMB excitation, whereas bright continuum sources are responsible for H_2CO absorption in the other regions. The two excitation mechanisms possibly produce different H_2CO intensities. The intensity of H_2CO absorption is related to the molecular density and background continuum sources. Using Origin Software to draw and calculate, the Pearson's correlation coefficients for line width between ^{12}CO emission and H_2CO absorption are 0.480, 0.556 and 0.478 for W3, DR21 and NGC2024 GMCs respectively (Fig. 11). The line width is greater for ^{12}CO emission than for H_2CO absorption on the whole. In general, there is good correlation between ^{12}CO and H_2CO clouds basing on these correlation coefficients.

Comparison of H_2CO and ^{12}CO contours and MSX data reveals great uniformity in morphology in the large area, especially between H_2CO and MSX data. The integrated intensity peaks are located at almost the same positions, but the ^{12}CO peaks are offset from the H_2CO peaks. MSX clouds are always located within star formation regions, where the hot core is the energy source for star formation. Basing above, under ambient conditions, H_2CO and ^{12}CO clouds form a blanket around star formation regions in morphology. This leads to a uniform structure that can be used as a tracer for star formation regions.

3.4. ^{12}CO peak offset from H_2CO and CBT

For the large-area distribution, ^{12}CO and H_2CO contours are fairly similar in morphology, but there is a peak offset (about $10'$ in Fig. 5(b) and 5(d)) for the small-area distribution. Heithausen et al. (1987) did not find a morphologic correlation between ^{12}CO and H_2CO data using a 100-m telescope, but Rodríguez et al. (2007) reported a discrepancy between ^{12}CO and H_2CO peaks toward the L1204 dust cloud using the Onsala 25-m telescope. Their H_2CO clouds were against the CMB, but our sources are against high CBT sources in HII regions. The background continuum temperature has a strong effect on the H_2CO distribution as we showed in Fig. 6, which reveals a fairly consistent morphology between H_2CO and the continuum. However, Fig. 5 shows that ^{12}CO peaks are offset from H_2CO peaks, although this offset is different from that observed by Rodríguez et al. (2007). Their H_2CO peaks were offset from the bright continuum source, while our ^{12}CO peaks are offset from the bright continuum source. Rodríguez et al. (2007) argued that the H_2CO peak offset arises from photodissociation in the UV interstellar radiation field. In our opinion, several factors explain the peak offset. First, the H_2CO distribution is strongly biased by the background CBT, while the strong HII region background has a relatively weak impact on ^{12}CO emission. Second, differences in star formation regions and evolution stages between sources will lead to discrepancy. Third, it is likely that H_2CO absorption is optically thin (< 0.188) and ^{12}CO emission is optically thick (Buckle et al. 2010), so ^{12}CO is a poor tracer for density. Finally, the different resolution may lead to discrepancy.

3.5. Statistical relationship between line width and intensity

Fig. 12 shows a statistical diagram of the relationship between line width and intensity for H_2CO absorption lines toward W49, W3, DR21/W75 and NGC2024/NGC2023 GMCs,

and for W43 GMC observations made by Wu et al. (2010) using the same dish. These data points are corresponding to 169 velocity components from our detected 86 H_2CO absorption lines. The statistical results show that the most (approximately 85.21%) of the velocity components of the H_2CO absorption lines are in the intensity range from -1.0 to 0 Jy and in the ΔV range 1.206 – 5.0 km s^{-1} .

In Fig. 12 the width for most H_2CO absorption lines is relatively narrow and may be narrower than the 1.206 km s^{-1} for the velocity channel. However, a few lines are rather wide, even up to 9.67 km s^{-1} . According to Bieging et al. (1982), the width of all H_2CO absorption lines observed in this paper far exceeds the thermal line width for any reasonable gas kinetic temperature (e.g. ΔV (thermal) = 0.3 km s^{-1} for H_2CO at 30 K), so the thermal broadening mechanism can be ignored. We suggest that line broadening is mainly the result of turbulence and velocity dispersion along any given line of sight. Thus, H_2CO line broadening should mainly reflect the blending of many velocity components.

4. SUMMARY

H_2CO absorption lines are important tracers for detecting the ambient conditions in star formation regions. So far very few people have carried out such large-scale H_2CO mapping as ours, especially for GMCs. We conducted discontinuous observations toward four GMCs from October 2009 to January 2011 using the Nanshan 25-m telescope. Long-time integration observations and analysis revealed the following results.

For W49, W3, DR21/W75 and NGC2024/NGC2023 GMCs, we observed 151 points using a beam width of $10'$ and integration for 9456 min, and found 86 H_2CO absorption lines and 16 $\text{H}110\alpha$ RRLs. We processed H_2CO absorption lines for four large-area mappings.

We described and gave some relevant physical parameters which are respectively flux, velocity, line width, intensity, CBT, apparent depth and column density for H_2CO absorp-

tion lines, $\text{H}110\alpha$ RRLs and continuum and clump's H_2 -mass for GMCs. Some good correlation coefficients between H_2CO and ^{12}CO were gained in terms of velocity components, line width and intensity.

In the large area, comparisons among H_2CO and ^{12}CO contours, the $8.28\text{-}\mu\text{m}$ MSX color map and CBT at 4.8 GHz revealed a consistent distribution. Regions with a high CBT had much higher collision excitation rates for H_2CO . However, in the small area, H_2CO and ^{12}CO peaks were not located at the same position. It is likely that the H_2CO distribution is strongly biased by the background CBT, while the strong HII region of the background has a relatively weak impact on ^{12}CO emission.

Many other results were observed for these four GMCs. E.g., W49B is a nonthermal SNR and has nearly the same velocity components as the thermal W49A. At the junction of two clouds for W3 GMC, we could not detect H_2CO absorption lines, whereas the ^{12}CO and MSX data were relatively strong. DR21/W75 GMCs had a velocity gradient, possibly arising from GMC rotation. It is possible that H_2CO absorption lines to the north of NGC2024/NGC2023 GMC arise from CMB excitation.

A statistical diagram of the relation between line width and intensity was constructed for H_2CO absorption lines. Approximately 85.21% of the velocity components of H_2CO absorption lines were distributed in the intensity range from -1.0 to 0 Jy and in the ΔV range 1.206 – 5.0 km s^{-1} .

We would like to thank all staff of Nanshan Observatory for observations throughout day and night. We are grateful for X. W. Zheng's assistance with providing useful insight into several aspects of this work. And we are grateful for T. M. Dame for providing and processing necessary ^{12}CO data. This work is supported by the National Natural Science Foundation of China (Grant Nos. 10778703 and 10873025) and the Program of the Light in China Western Region (LCWR; Nos. RCPY200605 and RCPY200706). MSX research has made use of the NASA/ IPAC Infrared Science Archive, which is operated by the Jet Propulsion Laboratory, California Institute of Technology, under contract with the National Aeronautics and Space Administration.

REFERENCES

- Araya, E., Hofner, P., Churchwell, E., & Kurtz, S. 2002, *ApJS*, 138, 63
 Araya, E., Hofner, P., Olmi, L., Kurtz, S., & Linz, H. 2006, *ApJ*, 132, 1851
 Bieging, J. H., Wilson, T. L., & Downes, D. 1982, *A&AS*, 49, 607
 Brogan, C. L., & Troland, T. H. 2001, *ApJ*, 550, 799
 Buckle, J. V., Curtis, E. I., Roberts, J. F., White, G. J., Hatchell, J., Brunt, C., Butner, H. M., Cavanagh, B., Chrysostomou, A., Davis, C. J., Duarte-Cabral, A., Etxaluze, M., di Francesco, J., Friberg, P., Friesen, R., Fuller, G. A., Graves, S., Greaves, J. S., Hogerheijde, M. R., Johnstone, D., Matthews, B., Matthews, H., Nutter, D., Rawlings, J. M. C., Richer, J. S., Sadavoy, S., Simpson, R. J., Tothill, N. F. H., Tsamis, Y. G., Viti, S., Ward-Thompson, D., Wouterloot, J. G. A., Yates, J. *MNRAS*, 2010, 401, 204
 Buhl, D., Snyder, L. E., Schwartz, P. R., & Barrett, A. H. 1969, *ApJ*, 158, L97
 Campbell, M. F., Hoffmann, W. F., Thronson, Jr., H. A., Niles, D., Nawfel, R., & Hawrylycz, M. 1982, *ApJ*, 261, 550
 Cohen, R. J., Matthews, N., Few, R. W. & Booth, R. S. 1983, *MNRAS*, 203, 1123
 Dame, T. M., Hartmann, Dap., & Thaddeus, P. 2001, *ApJ*, 547, 792
 de Pree, C. G., Mehringer, D. M., & Goss, W. M. 1997, *ApJ*, 482, 307
 Downes, D., Wilson, T. L., Bieging, J., & Wink, J. 1980, *A&AS*, 40, 379
 Dreher, J. W., Johnston, K. J., Welch, W. J., & Walker, R. C. 1984, *ApJ*, 283, 632
 Gaume, R. A., Johnston, K. J., & Wilson, T. L. 1992, *ApJ*, 388, 489
 Gwinn, C. R., Moran, J. M., & Reid, M. J. 1992, *ApJ*, 393, 149
 Heithausen, A., Mebold, U., de Vries, H. W. 1987 *A&A*, 179, 263
 Mangum, J. G. & Wootten, A. 1993, *ApJS*, 89, 123
 McKee, C. F., & Ostriker, E. C. 2007, *ARA&A*, 45, 565
 Menten, K. M., Reid, M. J., Forbrich, J., Brunthaler, A. 2007, *A&A*, 474, 515
 Palmer, P., Zuckerman, B., Buhl, D., & Snyder, L. E. 1969, *ApJ*, 156, L 147
 Pastchenko, M. I., & Slysh, V. I. 1973, *A&A*, 26, 349
 Piepenbrink, A., & Wendker, H. J. 1988, *A&A*, 191, 313
 Poeppel, W. G. L., Rohlf, K., Celnik, W. 1983, *A&A*, 126, 152
 Read, P. L. 1981, *MNRAS*, 194, 863
 Rodríguez, M. I., Allen, R. J., Wiklind, T. 2006 *ApJ*, 652, 1230
 Rodríguez, M. I., Wiklind, T., & Allen, R. J. 2007, *ApJ*, 663, 824
 Ruch, G. T., Jones, T. J., Woodward, C. E., Polomski, E. F., & Gehr, R. D. 2007, *ApJ*, 654, 338
 Scoville, N. Z., & Solomon, P. M. 1973, *ApJ*, 180, 31
 Shirley, Y. L., Evans, N. J., Young, K. E., Knez, C., Jaffe, D. T. 2003, *ApJS*, 149, 375
 Snyder, L. E., Buhl, D., Zuckerman, B., & Palmer, P. 1969, *Phys. Rev. Lett.*, 22, 679
 Sume, A., Downes, D., & Wilson, T. L. 1975, *A&A*, 39, 435
 Thompson, M. A., Hatchell, J., Walsh, A. J., Macdonald, G. H., & Millar, T. J. 2006, *A&A*, 453, 1003
 Thronson, H. A., Lada, C. J., & Hewagama, T. 1985, *ApJ*, 297, 662
 Watson, C., Araya, E., Sewilo, M., Churchwell, E., Hofner, P., Kurtz, S. 2003, *ApJ*, 587, 714
 Westerhout, G. 1958, *B. A. N.* 14, 215
 Wilson, T. L., Mauersberger, R. 1990, *A&A*, 239, 305
 Wu, G., Esimbek, J., & Zhou, J. J. 2010, *RAA*, 11, 63
 Xu, Y., Reid, M. J., Zheng, X. W., & Menten, K. M. 2006, *Science*, 311, 54

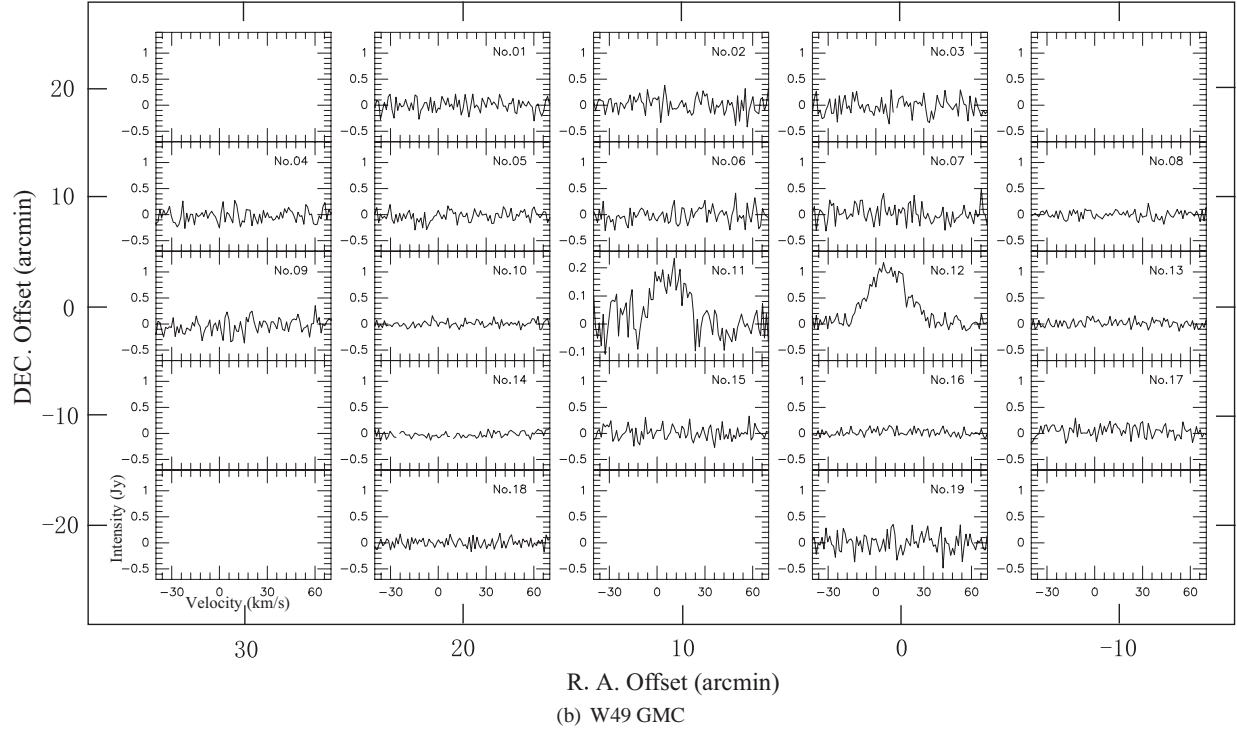
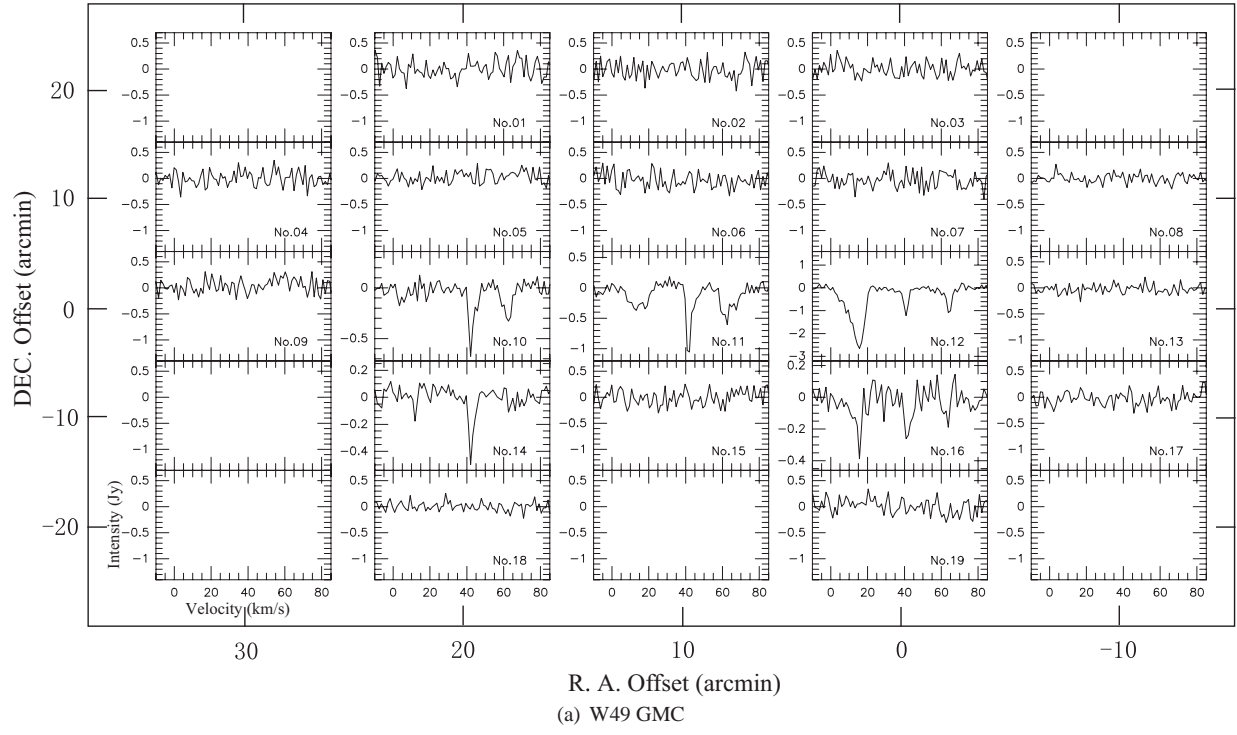


FIG. 1.— The spectral mosaic of (a) H_2CO absorption line and (b) $\text{H}110\alpha$ RRL toward W49 GMC.

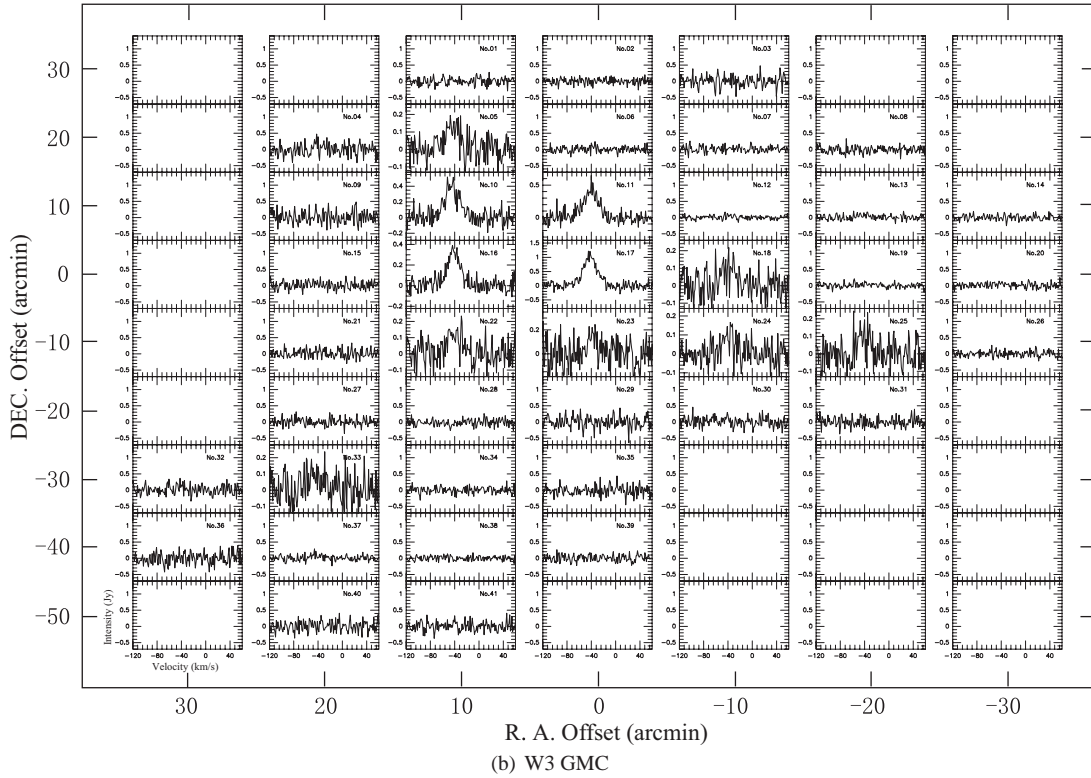
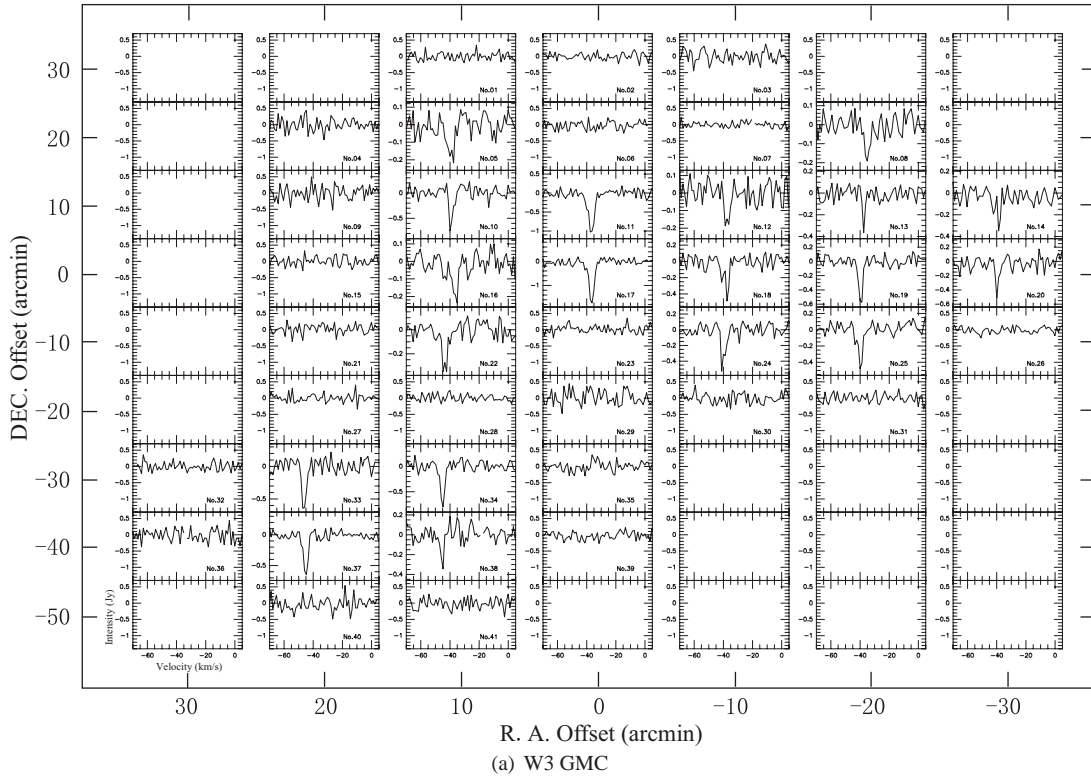


FIG. 2.— The spectral mosaic of (a) H_2CO absorption line and (b) $\text{H}110\alpha$ RRL toward W3 GMC.

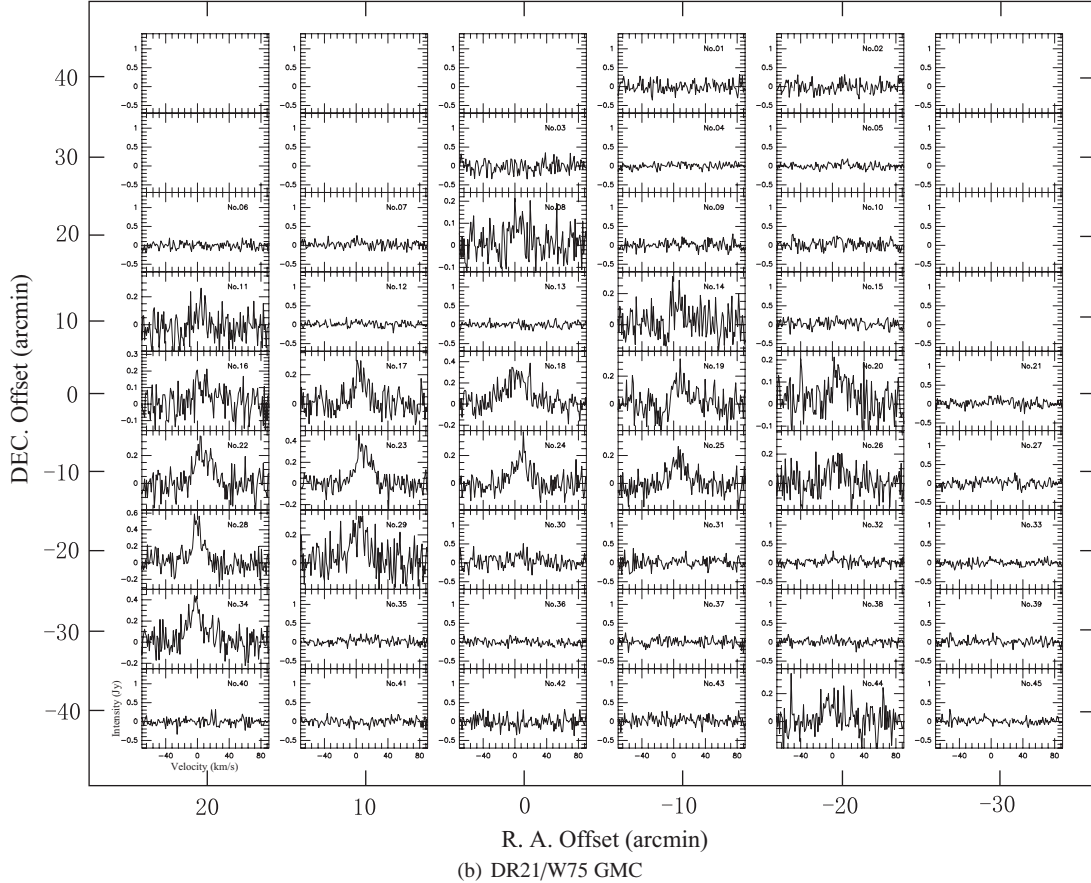
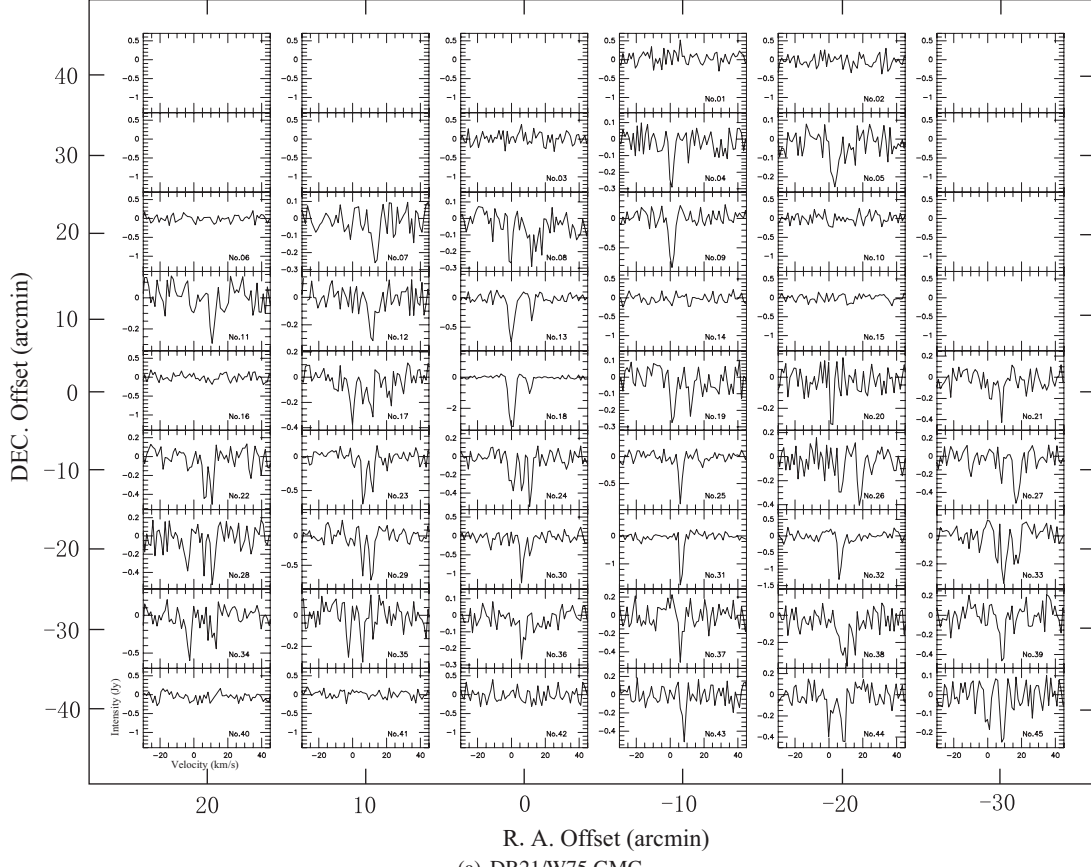
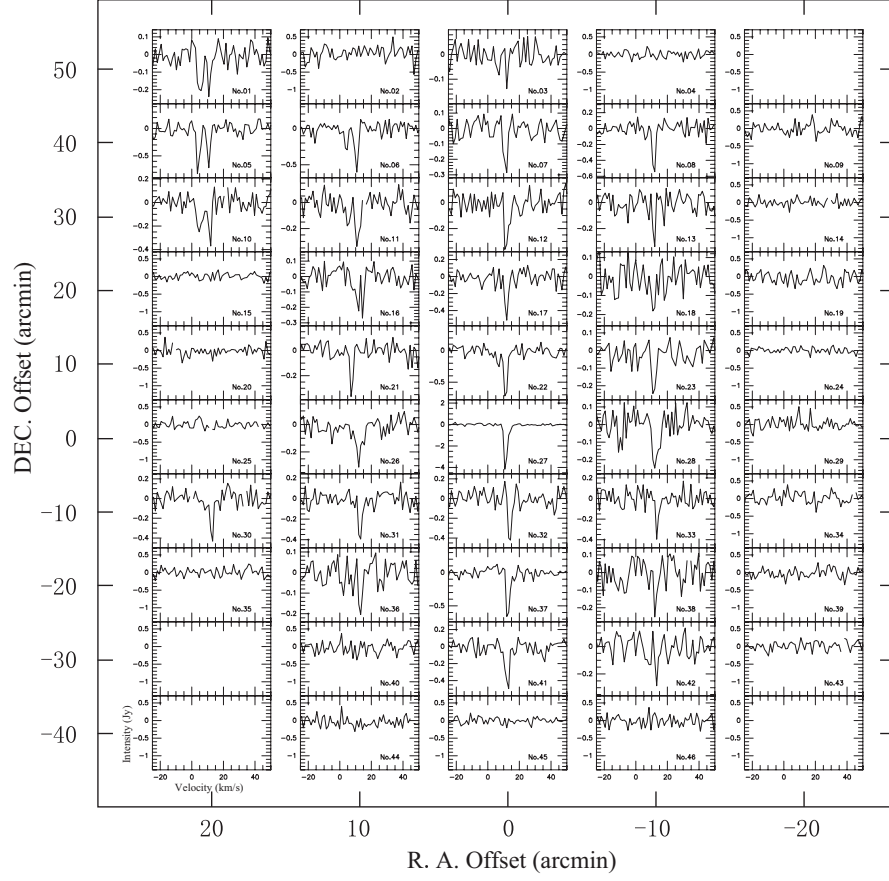
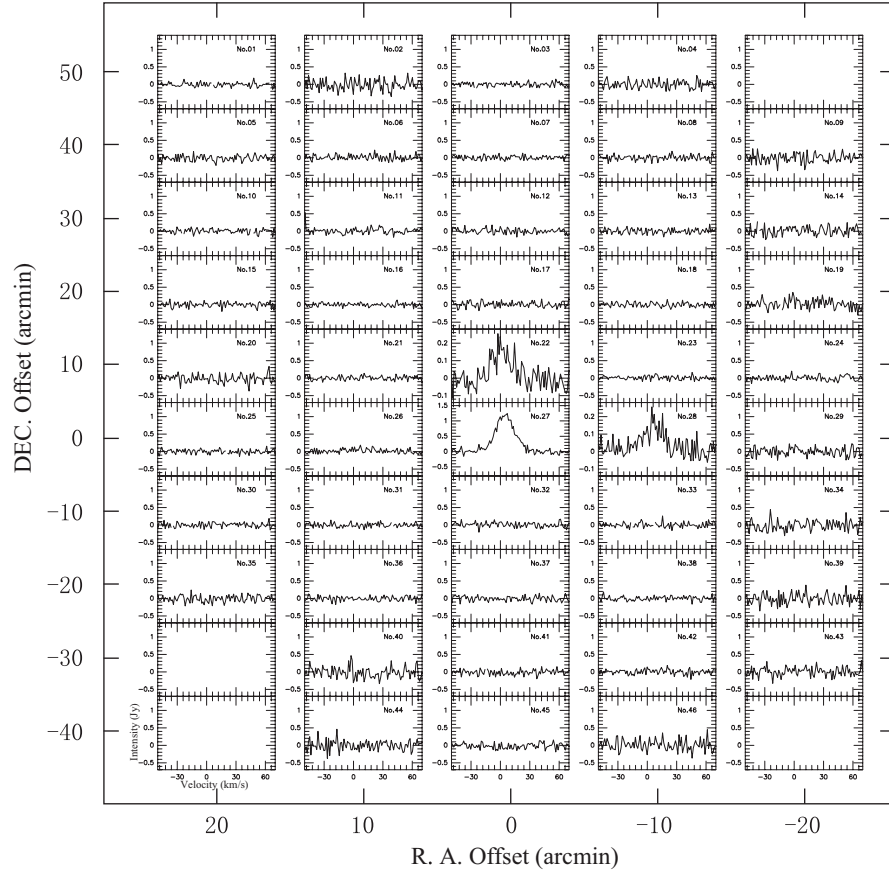


FIG. 3.— The spectral mosaic of (a) H_2CO absorption line and (b) $\text{H}110\alpha$ RRL toward DR21/W75 GMC.



(a) NGC2024/NGC2023 GMC



(b) NGC2024/NGC2023 GMC

FIG. 4.— The spectral mosaic of (a) H_2CO absorption line and (b) $\text{H}110\alpha$ RRL toward NGC2024/NGC2023 GMC.

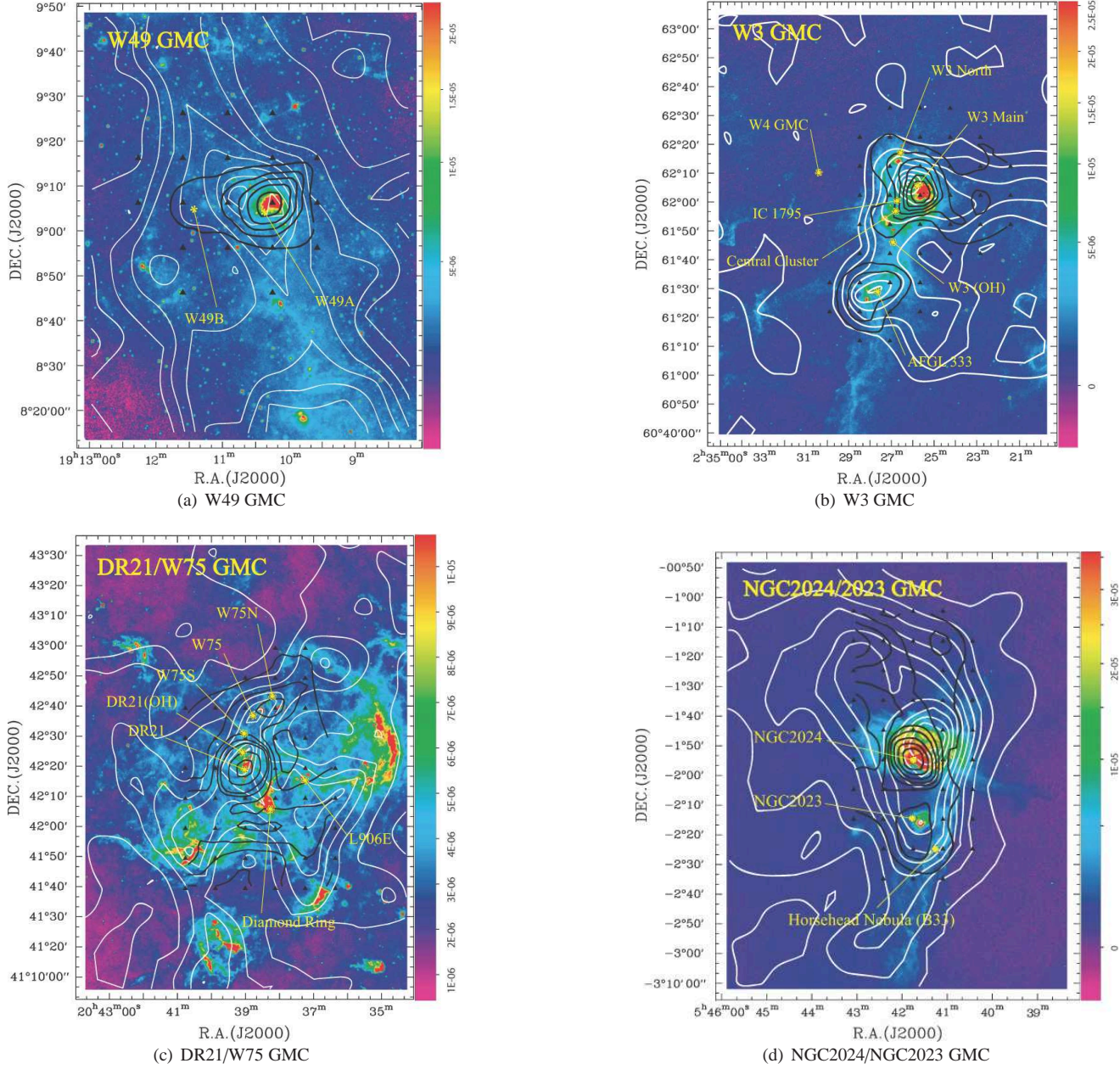


FIG. 5.— Contours and color-scale maps of integrated area toward W49, W3, DR21/W75 and NGC2024/NGC2023. The black contours, the white contours and the color-scale map respectively indicates the integrated flux intensity of the H₂CO absorption line, ¹²CO emission line and the mid-infrared 8.28-μm MSX source. Triangle symbols indicate the location what we surveyed and the coordinate of the offset (0, 0) position. (a), (0, 0): R.A. = 19^h10^m15^s.25, DEC. = 09°06′08″.4. Levels for black contours (H₂CO) with beam size 10′ are 29.15, 22.67, 16.19, 9.71 and 3.24 Jy km s⁻¹ from inside to outside, while 100 to 20 by -10 K km s⁻¹ for white contours (¹²CO) with beam size 8′. The corresponding velocity component is from -29.8 km s⁻¹ to 89.8 km s⁻¹ for H₂CO and ¹²CO. (b), (0, 0): R.A. = 02^h25^m38^s.79, DEC. = 62°02′22″.0. Levels for black contours (H₂CO) with beam size 10′ are 6.34, 5.22, 4.11, 2.99, 1.87 and 0.75 Jy km s⁻¹ from inside to outside, while 48 to 6 by -6 K km s⁻¹ for white contours (¹²CO) with beam size 8′. The corresponding velocity component is from -59.15 km s⁻¹ to -20.15 km s⁻¹ for H₂CO and ¹²CO. (c), (0, 0): R.A. = 20^h39^m01^s.23, DEC. = 42°19′33″.9. Levels for black contours (H₂CO) with beam size 10′ are 14.92, 10.00, 5.08, 3.85, 2.62, 1.39 and 0.16 Jy km s⁻¹ from inside to outside, while 81 to 4 by -11 K km s⁻¹ for white contours (¹²CO) with beam size 8′. The corresponding velocity component is from -15.4 km s⁻¹ to 25.6 km s⁻¹ for H₂CO and ¹²CO. (d), (0, 0): R.A. = 05^h41^m45^s.49, DEC. = -01°54′46″.8. Levels for black contours (H₂CO) with beam size 10′ are 8.69, 6.59, 4.50, 3.66, 2.83, 1.99, 1.15 and 0.31 Jy km s⁻¹ from inside to outside, while 124 to 4 by -12 K km s⁻¹ for white contours (¹²CO) with beam size 8′. The corresponding velocity component is from 0.33 km s⁻¹ to 20.48 km s⁻¹ for H₂CO and ¹²CO.

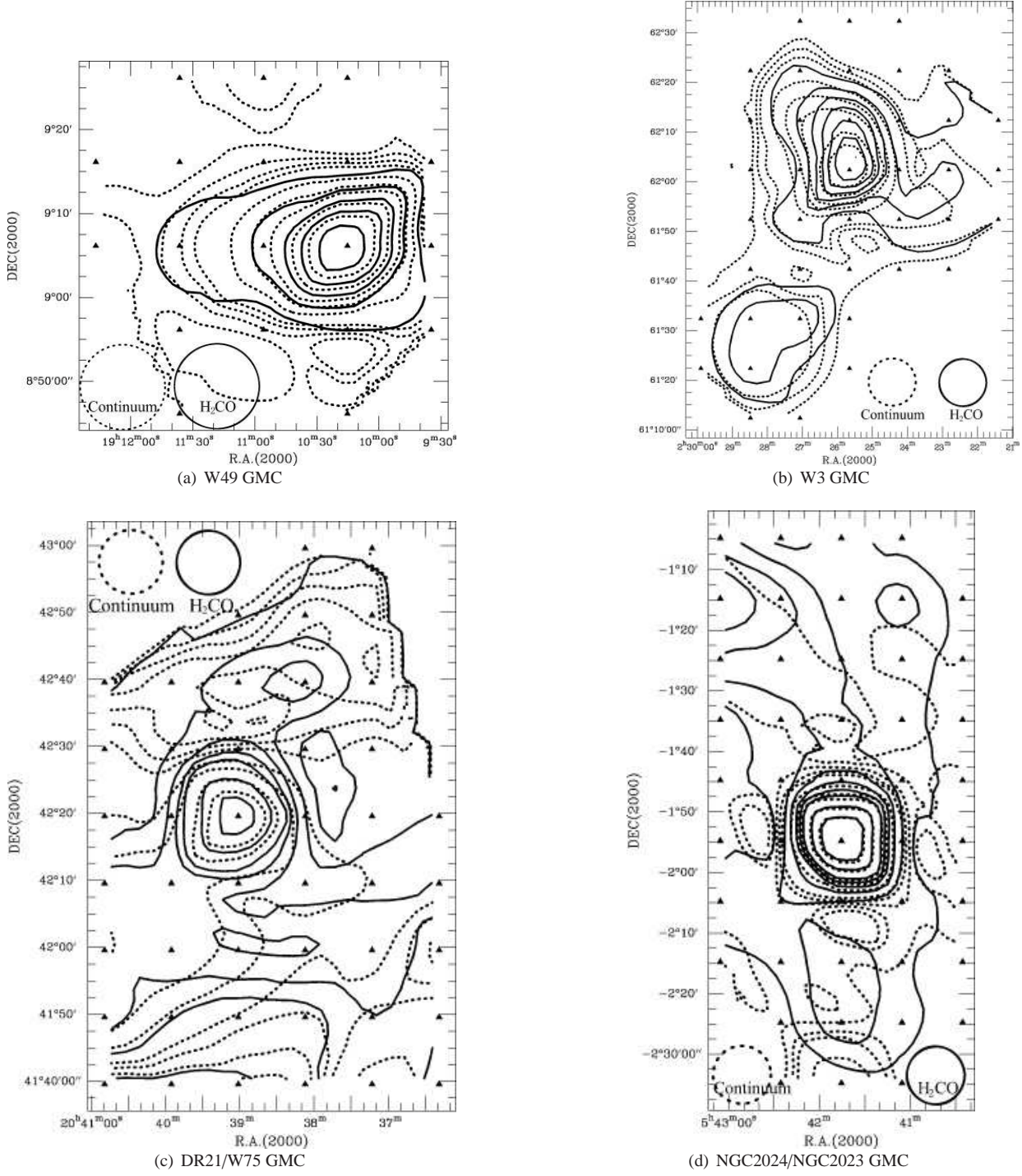


Fig. 6.— Integration intensity of H_2CO (Solid line) VS. Continuum brightness temperature of 4.85 GHz (Dotted line) for W49 GMC. For continuum brightness temperature, the contour levels from inside to outside are respectively (a) 4.601, 3.451, 2.301, 1.726, 1.150, 0.575, 0.431, 0.288 and 0.144 K, (b) 4.705, 3.529, 2.353, 1.765, 1.176, 0.588, 0.412 and 0.235 K, (c) 2.512, 1.884, 1.256, 0.942, 0.628, 0.534, 0.440, 0.345, 0.251, 0.157 and 0.063 K, and (d) 4.482, 3.361, 2.241, 1.681, 1.120, 0.560, 0.437, 0.314, 0.190 and 0.067 K, while they are same as Fig. 5 for integration intensity of H_2CO .

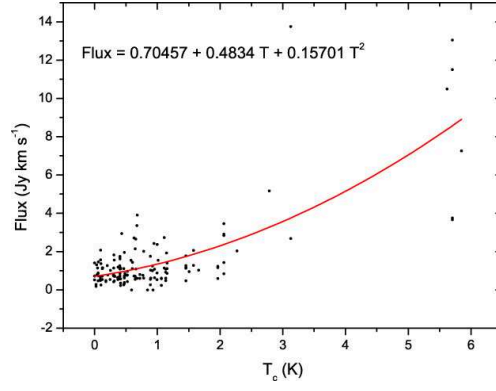


FIG. 7.— The relation between integration intensity of H_2CO and continuum brightness temperature of 4.85 GHz for W49, W3, DR21 and NGC2024 GMC.

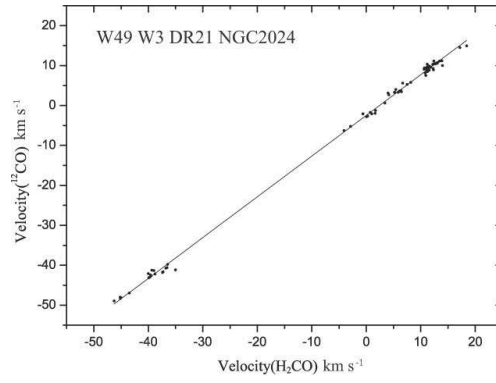


FIG. 8.— Correlation between velocity of H_2CO absorption line and ^{12}CO emission line for W49, W3, DR21/W75 and NGC2024/NGC2023 GMCs. From the data line, we can find the line passes through (0, 0) point and the points almost distribute on or near the line. So the relation between them is distinct.

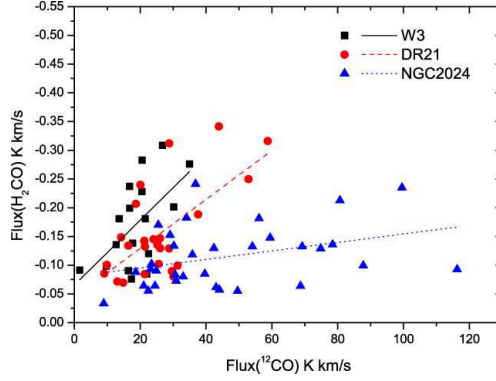


FIG. 9.— For W3, DR21/W75 and NGC2024/NGC2023 GMCs, the correlation between the H_2CO integration intensity and the ^{12}CO integration intensity.

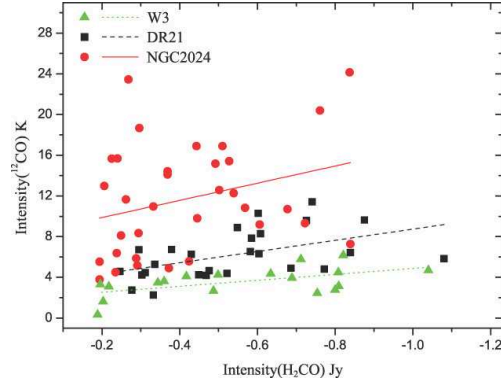


FIG. 10.— For W3, DR21/W75 and NGC2024/NGC2023 GMCs, correlation coefficient respectively being 0.558, 0.499 and 0.297 between intensities of ^{12}CO emission line and H_2CO absorption line.

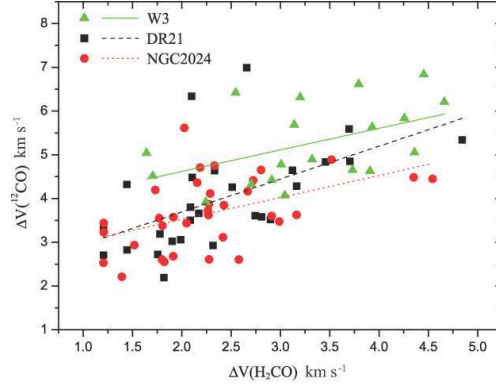


FIG. 11.— For W3, DR21/W75 and NGC2024/NGC2023 GMCs, correlation coefficient respectively being 0.480, 0.556 and 0.478 between line widths of ^{12}CO emission line and H_2CO absorption line.

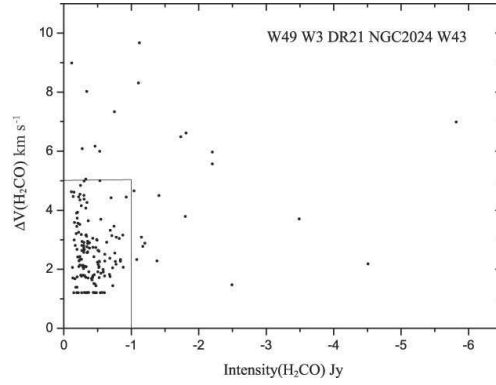


FIG. 12.— Correlation between line width and intensity of H_2CO absorption line at the each spectrum for W49, W3, DR21/W75 and NGC2024/NGC2023 GMCs and W43 GMC Wu et al. (2010). Each point comes from every velocity component of spectrum. The points in the range from -1.0 to 0 Jy and the ΔV range from 1.206 to 5 km s^{-1} hold 85.21% of all points.

TABLE 1 The relevant information of four GMCs.

Sources	ID (No.)	R.A.(J2000) (^h ^m ^s)	DEC.(J2000) ([°] ['] ^{''})	Distance (kpc)	Size($\alpha \times \delta$) (arcmin ²)	M(H_2) (M_\odot)	Int. time (minutes)	A/B/C	References
W49	12	19 10 15.25	09 06 08.4	11.4	50×50	2296910	966	19/5/2	(1), (5)
W3	17	02 25 38.79	62 02 22.0	1.95	70×90	71615	2370	41/19/4	(2), (5)
DR21	18	20 39 01.23	42 19 33.9	3.0	60×90	444774	2742	45/34/8	(3), (5)
NGC2024	27	05 41 45.49	-01 54 46.8	0.415	50×100	5609	3378	46/28/2	(4), (5)
Total					230×330		9456	151/86/16	

References: (1) Gwinn et al. (1992); (2) Xu et al. (2006); (3) Campbell et al. (1982); (4) Menten et al. (2007); (5) Bieging et al. (1982).

Notes:—— In Column 7 the clump's H_2 -masses ($M(H_2)$) are derived from Equation 5. In Column 9, A is the number of all observational positions toward the sources, B is the number of H_2CO absorption lines, and C is the number of $H110\alpha$ RRLs. Hence, the detection rate is 56.95% for H_2CO absorption lines and 10.60% for $H110\alpha$ RRLs.

TABLE 2 The parameters of W49 GMC.

W49		H ₂ CO								H110 α			
(1)	(2)	(3)	(4)	(5)	(6)	(7)	(8)	(9)	(10)	(11)	(12)	(13)	(14)
ID	Offset(α , δ)	Velocity	Flux	ΔV	Intensity	T_c	τ_{app}	$N(H_2CO)$	$N(H_2)$	Velocity	Flux	ΔV	Intensity
(No.)	(arcmin)	(km s ⁻¹)	(Jy km s ⁻¹)	(km s ⁻¹)	(Jy)	(K)		(10 ¹³ cm ⁻²)	(10 ²² cm ⁻²)	(km s ⁻¹)	(Jy km s ⁻¹)	(km s ⁻¹)	(Jy)
10	20, 0	4.733(0.68)	-0.73(0.20)	4.61(1.41)	-0.14(0.036)	0.406	0.012	0.503	0.403	N			
		42.18(0.11)	-1.72(0.15)	2.37(0.25)	-0.68(0.036)	0.406	0.058	1.286	1.029				
		45.51(0.32)	-0.58(0.13)	2.32(0.59)	-0.23(0.036)	0.406	0.019	0.418	0.334				
		62.09(0.30)	-1.75(0.20)	5.05(0.66)	-0.32(0.036)	0.406	0.027	1.270	1.016				
11	10, 0	12.68(0.69)	-2.91(0.52)	8.02(1.56)	-0.34(0.073)	2.060	0.013	0.978	0.782	7.52(1.47)	3.03(0.44)	19.08(2.74)	0.15(0.039)
		18.64(0.45)	-0.84(0.41)	2.94(1.12)	-0.26(0.073)	2.060	0.010	0.274	0.219				
		41.69(0.09)	-3.46(0.22)	2.77(0.23)	-1.17(0.073)	2.060	0.045	1.181	0.945				
		61.50(0.39)	-2.84(0.49)	5.00(0.77)	-0.53(0.073)	2.060	0.020	0.954	0.763				
		67.36(0.65)	-1.43(0.50)	4.50(1.74)	-0.29(0.073)	2.060	0.011	0.468	0.374				
12	0, 0	10.49(0.81)	-11.51(2.03)	9.67(0.90)	-1.12(0.099)	5.705	0.020	1.779	1.423	7.54(0.35)	31.39(0.82)	27.88(0.85)	1.06(0.104)
		15.88(0.16)	-13.05(2.03)	5.56(0.36)	-2.20(0.099)	5.705	0.039	2.028	1.622				
		40.86(0.11)	-3.67(0.31)	2.88(0.30)	-1.20(0.099)	5.705	0.021	0.568	0.454				
		64.25(0.12)	-3.76(0.34)	3.09(0.38)	-1.15(0.099)	5.705	0.020	0.584	0.467				
14	20, -10	11.99(0.57)	-0.26(0.14)	1.39(0.71)	-0.17(0.040)	0.102	0.018	0.236	0.189	N			
		42.36(0.16)	-1.37(0.18)	2.73(0.47)	-0.47(0.040)	0.102	0.051	1.302	1.042				
16	0, -10	12.54(1.92)	-1.10(0.41)	8.99(4.15)	-0.11(0.035)	0.414	0.009	0.766	0.613	N			
		15.66(0.30)	-0.58(0.23)	1.78(0.48)	-0.30(0.035)	0.414	0.025	0.417	0.333				
		41.93(0.43)	-1.14(0.23)	4.15(0.92)	-0.26(0.035)	0.414	0.022	0.841	0.673				
		60.91(0.82)	-0.23(0.26)	1.70(11.5)	-0.13(0.035)	0.414	0.011	0.171	0.137				
		63.63(0.70)	-0.36(0.23)	1.74(0.87)	-0.19(0.035)	0.414	0.016	0.257	0.206				

Notes: — Parameters listed about simultaneously observing H₂CO absorption line and H110 α RRL, and each one of both. The serial number and offset are indicated in Column one and two corresponding to spectra and color map. "N" indicates that the corresponding spectra could not be detected. These intensity data of H110 α RRL is not able to achieve 3 σ with "a" to line out, so we do not consider them as signal to analysis.

TABLE 3 The parameters of W3 GMC.

W3		H ₂ CO								H110 α			
(1)	(2)	(3)	(4)	(5)	(6)	(7)	(8)	(9)	(10)	(11)	(12)	(13)	(14)
ID	Offset(α , δ)	Velocity	Flux	ΔV	Intensity	T_c	τ_{app}	$N(H_2CO)$	$N(H_2)$	Velocity	Flux	ΔV	Intensity
(No.)	(arcmin)	(km s ⁻¹)	(Jy km s ⁻¹)	(km s ⁻¹)	(Jy)	(K)		(10 ¹³ cm ⁻²)	(10 ²² cm ⁻²)	(km s ⁻¹)	(Jy km s ⁻¹)	(km s ⁻¹)	(Jy)
05	10, 20	-38.73(0.28)	-1.03(0.13)	4.37(0.62)	-0.22(0.069)	0.892	0.014	0.558	0.446	-44.15(1.69)	3.67(0.50)	24.82(4.10)	0.13(0.056) ^a
08	-20, 20	-35.02(0.58)	-0.78(0.23)	3.90(1.29)	-0.18(0.022)	0.305	0.016	0.591	0.473	N			
10	10, 10	-39.37(0.18)	-2.04(0.27)	2.54(0.45)	-0.75(0.078)	2.269	0.027	0.644	0.515	-44.66(0.80)	11.87(0.69)	27.89(1.91)	0.40(0.080)
11	0, 10	-36.79(0.13)	-5.17(0.30)	4.66(0.33)	-1.04(0.104)	2.784	0.032	1.419	1.135	-40.79(0.72)	12.54(0.66)	27.79(1.74)	0.42(0.083)
12	-10, 10	-37.32(0.42)	-0.77(0.16)	3.73(0.73)	-0.19(0.031)	0.514	0.015	0.514	0.411	N			
13	-20, 10	-37.42(0.26)	-0.65(0.16)	1.70(0.39)	-0.36(0.002)	0.368	0.031	0.495	0.396	N			
14	-30, 10	-41.79(0.18)	-0.43(0.18)	1.20(3.01)	-0.34(0.001)	0.304	0.031	0.346	0.277	N			
		-38.25(0.20)	-0.73(0.17)	1.50(0.68)	-0.45(0.001)	0.304	0.041	0.576	0.461				
16	10, 0	-36.47(0.39)	-1.03(0.17)	4.45(0.95)	-0.21(0.035)	1.659	0.009	0.385	0.308	-41.70(0.62)	8.68(0.46)	24.30(1.59)	0.33(0.051)
17	0, 0	-36.57(0.09)	-7.26(0.38)	3.79(0.24)	-1.80(0.075)	5.850	0.031	1.103	0.882	-41.97(0.42)	28.59(0.95)	26.12(1.05)	1.03(0.121)
18	-10, 0	-40.86(0.31)	-0.64(0.18)	2.33(0.81)	-0.26(0.009)	0.957	0.016	0.340	0.272	-38.81(2.50)	3.09(0.56)	26.58(5.07)	0.11(0.065) ^a
		-37.15(0.16)	-1.08(0.16)	1.86(0.38)	-0.54(0.009)	0.957	0.033	0.569	0.455				
19	-20, 0	-39.54(0.12)	-1.96(0.16)	2.91(0.28)	-0.63(0.048)	0.475	0.051	1.390	1.112	N			
20	-30, 0	-39.78(0.20)	-1.19(0.22)	2.24(0.54)	-0.49(0.070)	0.375	0.042	0.889	0.711	N			
22	10, -10	-43.49(0.30)	-1.55(0.23)	4.25(0.82)	-0.34(0.066)	1.013	0.020	0.790	0.632	-40.71(2.10)	3.59(0.54)	26.59(3.98)	0.12(0.063) ^a
23	0, -10	N				0.844				-38.45(1.84)	2.66(0.71)	14.25(5.48)	0.17(0.080) ^a
24	-10, -10	-40.93(0.29)	-0.61(0.26)	1.20(2.09)	-0.48(0.016)	0.660	0.034	0.385	0.308	-39.34(1.91)	2.29(0.42)	20.81(4.50)	0.10(0.062) ^a
		-38.89(0.49)	-1.09(0.32)	3.15(0.82)	-0.32(0.016)	0.660	0.023	0.670	0.536				
25	-20, -10	-39.61(0.27)	-1.55(0.31)	3.00(0.87)	-0.48(0.049)	0.582	0.036	1.011	0.809	-41.93(2.42)	2.58(0.53)	21.30(4.02)	0.11(0.078) ^a
33	20, -30	-46.30(0.18)	-2.38(0.26)	3.14(0.38)	-0.71(0.055)	1.000	0.042	1.241	0.993	-46.05(4.29)	3.19(0.79)	32.19(8.33)	0.09(0.077) ^a
34	10, -30	-45.04(0.14)	-2.66(0.25)	3.04(0.34)	-0.82(0.054)	0.658	0.059	1.688	1.351	N			
37	20, -40	-45.14(0.14)	-2.43(0.20)	3.32(0.31)	-0.68(0.061)	0.948	0.041	1.290	1.032	N			
38	10, -40	-45.20(0.16)	-0.72(0.15)	1.64(0.64)	-0.41(0.016)	0.646	0.029	0.452	0.362	N			

Notes:— Parameters listed about simultaneously observing H₂CO absorption line and H110 α RRL, and each one of both. The serial number and offset are indicated in Column one and two corresponding to spectra and color map. "N" indicates that the corresponding spectra could not be detected. These intensity data of H110 α RRL is not able to achieve 3σ with "a" to line out, so we do not consider them as signal to analysis.

TABLE 4 The parameters of DR21/W75 GMC.

DR21		H ₂ CO								H110 α			
(1)	(2)	(3)	(4)	(5)	(6)	(7)	(8)	(9)	(10)	(11)	(12)	(13)	(14)
ID	Offset(α , δ)	Velocity	Flux	ΔV	Intensity	T_c	τ_{app}	$N(H_2CO)$	$N(H_2)$	Velocity	Flux	ΔV	Intensity
(No.)	(arcmin)	(km s ⁻¹)	(Jy km s ⁻¹)	(km s ⁻¹)	(Jy)	(K)		(10 ¹³ cm ⁻²)	(10 ²² cm ⁻²)	(km s ⁻¹)	(Jy km s ⁻¹)	(km s ⁻¹)	(Jy)
04	-10, 30	0.74(0.31)	-0.61(0.16)	2.10(0.66)	-0.27(0.019)	0.680	0.019	0.372	0.297	N			
05	-20, 30	3.43(0.46)	-1.26(0.24)	4.84(1.10)	-0.24(0.025)	0.402	0.020	0.913	0.730	N			
07	10, 20	13.97(0.43)	-0.69(0.19)	2.09(0.84)	-0.31(0.052)	0.393	0.026	0.514	0.411	N			
08	0, 20	-0.60(0.24)	-0.73(0.16)	2.08(0.54)	-0.33(0.019)	0.476	0.026	0.514	0.411	2.93(2.00)	2.09(0.47)	17.76(4.62)	0.11(0.055) ^a
		11.90(0.26)	-0.63(0.18)	2.13(0.85)	-0.28(0.019)	0.476	0.022	0.445	0.356				
		14.86(0.15)	-0.39(0.13)	1.20(13.1)	-0.30(0.019)	0.476	0.024	0.269	0.215				
		17.68(0.27)	-0.34(0.11)	1.20(5.50)	-0.26(0.019)	0.476	0.021	0.233	0.186				
09	-10, 20	1.01(0.16)	-2.94(0.30)	3.16(0.35)	-0.87(0.034)	0.434	0.073	2.168	1.735	N			
11	20, 10	10.82(0.33)	-0.85(0.20)	2.65(0.63)	-0.30(0.027)	0.406	0.025	0.624	0.499	4.70(1.79)	1.40(0.49)	10.35(4.29)	0.12(0.086) ^a
12	10, 10	11.23(0.29)	-1.11(0.21)	3.12(0.73)	-0.33(0.017)	0.467	0.026	0.775	0.620	N			
		15.16(0.68)	-0.27(0.16)	2.06(1.19)	-0.12(0.017)	0.467	0.010	0.185	0.148				
13	0, 10	0.00(0.11)	-2.72(0.18)	3.45(0.26)	-0.74(0.026)	0.628	0.054	1.757	1.406	N			
		12.33(0.18)	-0.73(0.11)	1.44(0.50)	-0.47(0.026)	0.628	0.034	0.461	0.369				
14	-10, 10	N				0.591				5.49(1.64)	2.52(0.49)	15.19(2.89)	0.15(0.097) ^a
16	20, 0	N				0.931				6.42(3.59)	3.07(0.79)	26.44(10.2)	0.10(0.070) ^a
17	10, 0	-0.24(0.24)	-1.08(0.19)	2.86(0.63)	-0.35(0.058)	1.136	0.019	0.516	0.413	4.73(0.96)	4.10(0.46)	17.85(2.46)	0.21(0.069)
		6.24(0.33)	-0.49(0.18)	2.09(1.12)	-0.22(0.058)	1.136	0.012	0.236	0.189				
		10.93(0.35)	-0.92(0.18)	2.91(0.64)	-0.29(0.058)	1.136	0.016	0.434	0.347				
		21.82(0.51)	-0.62(0.19)	3.21(1.07)	-0.18(0.058)	1.136	0.010	0.296	0.237				
18	0, 0	0.26(0.03)	-13.76(0.27)	3.70(0.07)	-3.49(0.164)	3.128	0.103	3.590	2.872	2.14(1.32)	9.74(0.73)	34.96(3.10)	0.26(0.085)
		10.91(0.10)	-2.69(0.22)	2.33(0.20)	-1.08(0.164)	3.128	0.031	0.675	0.540				
19	-10, 0	1.63(0.26)	-0.88(0.16)	2.80(0.57)	-0.29(0.011)	0.996	0.017	0.447	0.358	8.11(1.64)	3.20(0.53)	17.51(3.27)	0.17(0.069) ^a
		12.18(0.28)	-0.54(0.15)	2.14(0.79)	-0.23(0.011)	0.996	0.013	0.271	0.217				
20	-20, 0	1.70(0.07)	-0.77(0.12)	1.20(2.55)	-0.60(0.000)	0.772	0.040	0.452	0.362	9.73(2.22)	3.54(0.61)	25.98(5.34)	0.12(0.054) ^a
21	-30, 0	1.77(0.34)	-0.61(0.25)	2.43(1.56)	-0.23(0.010)	0.724	0.016	0.356	0.285	N			
		8.22(0.22)	-0.81(0.17)	1.78(0.40)	-0.43(0.010)	0.724	0.029	0.491	0.393				
22	20, -10	-2.70(0.74)	-0.48(0.22)	2.99(1.25)	-0.15(0.021)	1.455	0.007	0.200	0.160	6.96(1.18)	5.88(0.57)	23.66(2.42)	0.23(0.067)
		6.49(0.16)	-1.27(0.21)	2.26(0.53)	-0.52(0.021)	1.455	0.025	0.528	0.423				
		10.60(0.18)	-1.13(0.19)	2.06(0.35)	-0.51(0.021)	1.455	0.024	0.472	0.378				
23	10, -10	6.44(0.10)	-1.78(0.15)	2.17(0.17)	-0.77(0.049)	1.455	0.037	0.756	0.605	8.86(0.71)	7.48(0.50)	21.37(1.62)	0.32(0.064)
		11.55(0.13)	-1.18(0.18)	1.90(0.42)	-0.58(0.049)	1.455	0.028	0.496	0.397				
24	0, -10	0.42(0.25)	-1.40(0.19)	3.64(0.50)	-0.36(0.045)	1.156	0.020	0.669	0.535	8.14(1.07)	4.33(0.46)	20.52(2.67)	0.19(0.063)
		6.36(0.16)	-0.86(0.14)	1.81(0.38)	-0.44(0.045)	1.156	0.024	0.408	0.326				
		11.21(0.11)	-1.11(0.12)	1.44(0.47)	-0.72(0.045)	1.156	0.040	0.535	0.428				
25	-10, -10	6.04(0.09)	-1.93(0.17)	2.06(0.19)	-0.88(0.030)	1.148	0.049	0.943	0.754	6.04(1.20)	3.68(0.46)	20.14(3.06)	0.17(0.063) ^a
26	-20, -10	6.99(0.32)	-1.00(0.22)	2.76(0.66)	-0.34(0.053)	0.922	0.021	0.538	0.430	4.51(2.09)	2.80(0.57)	19.54(3.99)	0.13(0.072) ^a
		18.41(0.26)	-1.25(0.22)	2.74(0.52)	-0.43(0.053)	0.922	0.026	0.677	0.542				
27	-30, -10	7.88(0.39)	-0.56(0.22)	1.21(25.2)	-0.43(0.040)	0.649	0.031	0.349	0.279	N			
		17.17(0.22)	-2.15(0.25)	3.69(0.47)	-0.54(0.040)	0.649	0.039	1.343	1.074				
28	20, -20	-4.09(0.44)	-1.16(0.32)	2.89(0.94)	-0.37(0.027)	1.964	0.015	0.396	0.317	0.14(0.68)	7.20(0.71)	14.87(1.97)	0.45(0.095)
		6.11(0.36)	-0.60(0.21)	1.20(1.11)	-0.46(0.027)	1.964	0.018	0.205	0.164				
		11.14(0.20)	-1.23(0.28)	1.98(0.59)	-0.58(0.027)	1.964	0.023	0.427	0.342				
29	10, -20	5.87(0.16)	-1.28(0.21)	1.75(0.25)	-0.68(0.013)	1.577	0.031	0.511	0.409	3.59(1.56)	6.41(0.90)	23.39(4.18)	0.25(0.080)
		11.18(0.14)	-2.07(0.26)	2.31(0.36)	-0.83(0.013)	1.577	0.038	0.827	0.661				
30	0, -20	6.17(0.11)	-2.73(0.33)	2.03(0.32)	-1.26(0.111)	1.111	0.072	1.369	1.095	N			
		11.15(0.25)	-1.14(0.32)	1.77(0.89)	-0.60(0.111)	1.111	0.034	0.558	0.446				
31	-10, -20	6.45(0.04)	-3.91(0.23)	1.47(0.42)	-2.49(0.105)	0.682	0.188	2.603	2.083	N			
32	-20, -20	6.39(0.09)	-3.36(0.30)	2.28(0.28)	-1.38(0.126)	0.674	0.101	2.155	1.724	N			
33	-30, -20	5.36(0.15)	-0.44(0.16)	1.20(3.14)	-0.34(0.051)	0.523	0.026	0.296	0.237	N			
		9.57(0.30)	-0.97(0.21)	2.58(0.59)	-0.35(0.051)	0.523	0.027	0.655	0.524				
		16.97(0.58)	-0.78(0.23)	3.56(0.90)	-0.20(0.051)	0.523	0.015	0.514	0.411				
34	20, -30	-2.89(0.20)	-1.62(0.25)	2.51(0.46)	-0.60(0.115)	0.404	0.051	1.199	0.960	-2.69(1.15)	7.54(0.88)	21.89(3.56)	0.32(0.085)
		12.16(0.39)	-1.09(0.24)	2.71(0.60)	-0.37(0.115)	0.404	0.031	0.791	0.633				
35	10, -30	-2.49(0.29)	-0.62(0.15)	2.08(0.43)	-0.28(0.010)	1.064	0.016	0.310	0.248	N			
		5.64(0.24)	-0.59(0.14)	1.73(0.55)	-0.32(0.010)	1.064	0.018	0.295	0.236				
		12.31(0.29)	-0.24(0.12)	1.20(0.68)	-0.19(0.010)	1.064	0.011	0.121	0.097				
36	0, -30	6.36(0.44)	-0.62(0.17)	2.33(0.92)	-0.25(0.067)	0.897	0.015	0.337	0.270	N			
37	-10, -30	6.08(0.23)	-0.95(0.23)	1.71(0.46)	-0.52(0.009)	1.507	0.024	0.391	0.313	N			
38	-20, -30	8.12(0.57)	-1.76(0.36)	6.09(1.42)	-0.27(0.025)	0.890	0.017	0.957	0.765	N			
		10.66(0.49)	-0.27(0.13)	1.20(0.73)	-0.21(0.025)	0.890	0.013	0.146	0.117				
		15.10(0.11)	-0.56(0.13)	1.20(1.55)	-0.43(0.025)	0.890	0.027	0.302	0.241				
39	-30, -30	8.71(0.25)	-1.44(0.28)	2.61(0.63)	-0.51(0.037)	0.606	0.038	0.921	0.737	N			
43	-10, -40	8.18(0.24)	-1.15(0.26)	2.08(0.53)	-0.52(0.015)	0.129	0.055	1.074	0.859	N			
44	-20, -40	0.11(0.24)	-0.73(0.21)	1.68(0.61)	-0.41(0.065)	0.000	0.049	0.769	0.616	-2.61(2.80)	3.03(0.75)	22.15(7.36)	0.12(0.075) ^a
		8.59(0.24)	-1.41(0.24)	2.63(0.54)	-0.50(0.065)	0.000	0.060	1.477	1.182				
45	-30, -40	0.18(0.48)	-0.50(0.16)	2.80(0.74)	-0.16(0.036)	0.094	0.017	0.450	0.360	N			
		8.91(0.09)	-0.57(0.12)	1.20(5.32)	-0.45(0.036)	0.094	0.049	0.551	0.441				

Notes:— Parameters listed about simultaneously observing H₂CO absorption line and H110 α RRL, and each one of both. The serial number and offset are indicated in Column one and two corresponding to spectra and color map. "N" indicates that the corresponding spectra could not be detected. These intensity data of H110 α RRL is not able to achieve 3 σ with "a" to line out, so we do not consider them as signal to analysis.

TABLE 5 The parameters of NGC2024/2023 GMC.

NGC2024		H ₂ CO								H110 α			
(1) ID	(2) Offset(α, δ)	(3) Velocity (km s ⁻¹)	(4) Flux (Jy km s ⁻¹)	(5) ΔV (km s ⁻¹)	(6) Intensity (Jy)	(7) T_c (K)	(8) τ_{app}	(9) $N(H_2CO)$ (10 ¹³ cm ⁻²)	(10) $N(H_2)$ (10 ²² cm ⁻²)	(11) Velocity (km s ⁻¹)	(12) Flux (Jy km s ⁻¹)	(13) ΔV (km s ⁻¹)	(14) Intensity (Jy)
01	20, 50	5.40(0.35)	-0.88(0.17)	3.51(0.64)	-0.23(0.032)	0.058	0.026	0.842	0.674	N			
03	0, 50	10.99(0.26)	-0.48(0.13)	1.80(0.61)	-0.24(0.032)	0.058	0.027	0.451	0.361	N			
		7.49(0.29)	-0.19(0.07)	1.20(1.74)	-0.14(0.001)	0.024	0.016	0.180	0.144				
		12.27(0.21)	-0.29(0.08)	1.39(0.42)	-0.19(0.001)	0.024	0.022	0.284	0.227				
05	20, 40	4.01(0.14)	-2.08(0.25)	2.33(0.39)	-0.83(0.092)	0.095	0.092	2.016	1.612	N			
		10.68(0.14)	-1.57(0.20)	2.04(0.26)	-0.72(0.092)	0.095	0.079	1.521	1.217				
06	10, 40	4.13(0.19)	-0.75(0.18)	1.91(0.72)	-0.37(0.029)	0.060	0.041	0.742	0.594	N			
		10.61(0.14)	-1.46(0.18)	2.27(0.30)	-0.60(0.029)	0.060	0.068	1.449	1.159				
07	0, 40	11.28(0.26)	-0.80(0.15)	2.57(0.51)	-0.29(0.050)	0.038	0.033	0.796	0.637	N			
08	-10, 40	11.43(0.08)	-1.31(0.15)	1.82(0.36)	-0.67(0.002)	0.034	0.078	1.337	1.070	N			
10	20, 30	5.17(0.49)	-1.15(0.22)	4.54(1.10)	-0.23(0.028)	0.125	0.024	1.025	0.820	N			
		11.47(0.27)	-0.73(0.25)	1.20(34.1)	-0.56(0.028)	0.125	0.059	0.671	0.537				
11	10, 30	5.28(0.52)	-0.55(0.17)	2.66(1.18)	-0.19(0.040)	0.125	0.020	0.495	0.396	N			
		11.23(0.27)	-1.11(0.18)	3.16(0.58)	-0.33(0.040)	0.125	0.035	1.028	0.823				
12	0, 30	11.79(0.31)	-1.14(0.20)	2.91(0.69)	-0.36(0.099)	0.049	0.041	1.111	0.889	N			
13	-10, 30	11.46(0.08)	-0.69(0.12)	1.20(1.29)	-0.53(0.000)	0.092	0.058	0.654	0.523	N			
16	10, 20	11.48(0.13)	-0.49(0.12)	1.77(1.21)	-0.26(0.015)	0.180	0.026	0.431	0.345	N			
		14.74(0.14)	-0.44(0.09)	1.20(0.55)	-0.34(0.015)	0.180	0.034	0.383	0.307				
17	0, 20	11.79(0.16)	-1.27(0.17)	2.27(0.34)	-0.52(0.024)	0.201	0.052	1.100	0.880	N			
18	-10, 20	11.11(0.40)	-0.53(0.17)	2.41(0.97)	-0.20(0.023)	0.001	0.023	0.531	0.425	N			
21	10, 10	7.51(0.15)	-0.78(0.12)	1.73(0.44)	-0.42(0.005)	0.300	0.038	0.621	0.497	N			
22	0, 10	6.67(0.23)	-0.62(0.17)	2.02(0.74)	-0.29(0.008)	0.783	0.019	0.362	0.289	1.08(1.28)	3.59(0.45)	20.38(2.87)	0.16(0.067) ^a
		11.26(0.08)	-2.02(0.14)	2.27(0.22)	-0.83(0.008)	0.783	0.056	1.185	0.948				
23	-10, 10	11.37(0.29)	-0.79(0.15)	2.80(0.57)	-0.26(0.018)	0.211	0.025	0.664	0.531	N			
26	10, 0	12.19(0.66)	-0.85(0.29)	2.72(1.66)	-0.29(0.081)	0.485	0.023	0.586	0.469	N			
27	0, 0	11.21(0.02)	-10.49(0.27)	2.18(0.08)	-4.51(0.292)	5.619	0.082	1.687	1.350	4.69(0.18)	28.03(0.47)	22.27(0.44)	1.18(0.080)
28	-10, 0	12.53(0.40)	-1.11(0.19)	4.35(0.75)	-0.24(0.044)	0.603	0.018	0.716	0.573	5.65(1.24)	3.69(0.39)	22.77(2.88)	0.15(0.049)
30	20, -10	12.68(0.12)	-1.02(0.16)	1.91(0.51)	-0.50(0.020)	0.254	0.047	0.850	0.680	N			
31	10, -10	12.82(0.17)	-1.14(0.16)	2.42(0.41)	-0.44(0.049)	0.305	0.040	0.908	0.726	N			
32	0, -10	13.89(0.16)	-1.17(0.16)	2.15(0.38)	-0.51(0.041)	0.392	0.043	0.878	0.702	N			
33	-10, -10	13.48(0.24)	-0.71(0.15)	1.51(0.68)	-0.44(0.004)	0.324	0.039	0.558	0.446	N			
36	10, -20	13.01(0.28)	-0.55(0.12)	2.28(0.47)	-0.22(0.023)	0.249	0.021	0.442	0.354	N			
37	0, -20	12.66(0.10)	-1.83(0.15)	2.26(0.24)	-0.76(0.102)	0.307	0.070	1.483	1.186	N			
38	-10, -20	12.40(0.19)	-0.47(0.14)	1.20(28.9)	-0.36(0.000)	0.314	0.032	0.364	0.291	N			
41	0, -30	12.34(0.22)	-1.56(0.23)	2.98(0.51)	-0.49(0.071)	0.313	0.044	1.240	0.992	N			
42	-10, -30	13.13(0.29)	-0.55(0.15)	1.80(0.44)	-0.28(0.004)	0.371	0.024	0.406	0.325	N			

Notes:— Parameters listed about simultaneously observing H₂CO absorption line and H110 α RRL, and each one of both. The serial number and offset are indicated in Column one and two corresponding to spectra and color map. "N" indicates that the corresponding spectra could not be detected. These intensity data of H110 α RRL is not able to achieve 3 σ with "a" to line out, so we do not consider them as signal to analysis.